Conceptual study on nucleation burst evolution in the convective boundary layer ? Part II: Meteorological characterization

O. Hellmuth

▶ **To cite this version:**

O. Hellmuth. Conceptual study on nucleation burst evolution in the convective boundary layer ? Part II: Meteorological characterization. Atmospheric Chemistry and Physics Discussions, 2005, 5 (6), pp.11489-11515. hal-00301917

HAL Id: hal-00301917
https://hal.science/hal-00301917

Submitted on 10 Nov 2005

HAL is a multi-disciplinary open access archive for the deposit and dissemination of scientific research documents, whether they are published or not. The documents may come from teaching and research institutions in France or abroad, or from public or private research centers.

L'archive ouverte pluridisciplinaire **HAL**, est destinée au dépôt et à la diffusion de documents scientifiques de niveau recherche, publiés ou non, émanant des établissements d'enseignement et de recherche français ou étrangers, des laboratoires publics ou privés.

Atmos. Chem. Phys. Discuss., 5, 11489–11515, 2005
www.atmos-chem-phys.org/acpd/5/11489/
SRef-ID: 1680-7375/acpd/2005-5-11489
European Geosciences Union

Atmospheric Chemistry and Physics Discussions

Conceptual study on nucleation burst evolution in the convective boundary layer – Part II: Meteorological characterization

O. Hellmuth

Modelling Department, Institute for Tropospheric Research, Permoser Str. 15, 04318 Leipzig, Germany

Received: 1 August 2005 – Accepted: 17 October 2005 – Published: 10 November 2005

Correspondence to: O. Hellmuth (olaf@tropos.de)

© 2005 Author(s). This work is licensed under a Creative Commons License.

Abstract

While in part I of the present paper a revised columnar high-order modelling approach to investigate gas-aerosol interactions in the convective boundary layer (CBL) was deduced, in the present part the model capability to predict the evolution of meteorological CBL parameters is demonstrated. Based on a model setup to simulate typical CBL conditions, predicted first-, second- and third-order moments were shown to agree very well with those obtained from in situ and remote sensing turbulence measurements such as aircraft, SODAR and LIDAR measurements as well as with those derived from ensemble-averaged large-eddy simulations and wind tunnel experiments. The results show that the model is able to predict the meteorological CBL parameters, required to verify or falsify, respectively, previous hypothesis on the interaction between CBL turbulence and new particle formation.

1. Introduction

In part I of the present paper a high-order model was deduced to simulate gas-aerosol interactions. Here, simulation results of the meteorological conditions will be presented, under which new particle formation (NPF) in the anthropogenically influenced convective boundary layer (CBL) can be obeserved. Based on a compilation of available data from the literature, predicted first-, second- and third-order moments will be evaluated using data from previous measurements and simulations of CBL turbulence. A comprehensive model verification and/or validation would require a dedicated boundary layer surveying including vertical profiling of higher-order moments of meteorological parameters. This is beyond the scope of the present paper. Instead of this, here we will focus on a comparison with previous observations that are typical for the CBL evolution. The model is assessed with respect to its capability to reproduce typical CBL features that are reported in the literature to frequently occur during daytime NPF events.

ACPD

5, 11489–11515, 2005

2. Model setup

One way to perform a modelling study on gas-aerosol interactions in a turbulent CBL flow is to empirically prescribe the meteorological parameters, e.g., such as realized in the approach of Verver et al. (1997). In their second-order turbulence modelling study on chemical reactions, the authors specified stationary profiles for temperature and temperature variance in the well-mixed layer as well as entrainment and surface fluxes for the boundary conditions. Doing this, an explicit simulation of the evolution of the boundary layer can be avoided. In opposite to this, in the present study the CBL evolution will be explicitely simulated.

The initial profiles of potential temperature and water vapour mixing ratio are shown in Fig. 1a. At the beginning, the atmosphere is stably stratified. The components of the geostrophic wind are considered to be time-independent with u_g=5 m/s, v_g=0 m/s. The large-scale subsidence was adjusted according to Fig. 1b, whereas the vertical velocity was kept constant over the period of time integration. The model was integrated from 03:00 to 21:00 LST (Local Standard Time).

3. Evolution of the convective boundary layer

3.1. General picture

The typical evolution of the CBL in high pressure regions over land is previously described, e.g., by Stull (1997, p. 9–19, Fig. 1.7). The author distinguishes three major parts of the boundary layer: (a) a very turbulent mixed layer; (b) a less-turbulent residual layer containing former mixed-layer air; (c) a nocturnal stable boundary layer of sporadic turbulence. Depending on the Bowen ratio and soil properties, the Prandtl layer is heated after sunrise by the upward directed turbulent flux of sensible heat. Afterwards, the heated air starts rising resulting in the growth of the mixing layer height (MLH). The most energy-containing eddies are able to penetrate into the free

troposphere causing entrainment. When the turbulent heat flux changes its sign, the buoancy-induced turbulence rapidly weakens, the mixing layer collapses and a residual layer forms. The classical CBL picture was frequently confirmed by observations, e.g., by Cohn and Angevine (2000) using ground-based high-resolution Doppler-LIDAR, aerosol backscatter LIDAR, and wind profiler. Nilsson et al. (2001) found new particle formation (NPF) events preferentially occuring in boundary layers essentially following that pattern. During the BIOFOR experiment in spring 1999, NPF was frequently observed in CBLs formed in Arctic and polar air masses during cold air outbreaks favouring clear-sky conditions and subsequently, leading to an insolation-forced boundary layer evolution. Such events were typically associated with rapid development and growth of a mixed layer, subsequent convection and strong entrainment. It will be shown, that the boundary layer considered here depicts in general that situation.

3.2. First-order moments

Horizontal wind components (Fig. 2a, b): The wind field is forced by a time-independent x-component of the geostrophic wind at all heights. Due to frictional forcing induced by the Reynolds stresses the $\overline{u}$ wind decreases from the mixing layer height (MLH) toward the ground, while the $\overline{v}$ wind steadily increases in the course of the day and throughout the CBL due to Coriolis forcing. Consequently, an Ekman helix forms. The MLH evolution can be clearly seen from the narrow transition zone separating the geostrophic wind regime from the turbulence regime below. When the mixing layer collapses in the evening, a weakly supergeostrophic $\overline{u}$ wind starts to form in the residual layer.

Potential temperature and temperature (Fig. 2c, d): Starting with a stable temperature stratification at night, the temperature in the Prandtl layer assumes its minimum in the early morning before sunrise. This is a result of radiative surface cooling followed by downward directed sensible heat flux. At that time, NPF is favoured to occur as will be shown in part III. After sunrise, the surface temperature starts to increase due to the increasing sensible heat flux disfavouring NPF. As a result, during the day a mixed layer with increasing potential temperature forms. The large-scale subsidence has a

strong stabilization effect, hence tending to constrain the CBL evolution and MLH. In the evening, the atmospheric stratification becomes more and more stable due to radiative surface cooling followed by downward directed turbulent heat flux in the Prandtl layer.

Water vapour mixing ratio and relative humidity (Fig. 2e, f): The latent heat flux assumes its minimum just before sunrise, hence leading to the maximum of the water vapour mixing ratio in the Prandtl layer at that time. The near-surface air can easily become saturated with water vapour leading to the formation of radiation fog and favouring NPF owing to high relative humidity. Lateron, the evolution of relative humidity is controlled by the sensible and latent heat flux in the Prandtl layer as well as by CBL heating/drying by large-scale subsidence and net radiative heating throughout the CBL. Due to CBL warming and drying the relative humidity decreases during the course of the day, hence disfavouring NPF.

3.3. Second-order moments

3.3.1. Components of the Reynolds stress tensor (Fig. 3a–f)

(a) Simulation results

The variances $\overline{u'u'}$ (Fig. 3a) and $\overline{v'v'}$ (Fig. 3d), respectively, exceed their maxima at the first half level, i.e., at the surface, resulting from surface momentum friction. From there, the variances of horizontal velocity components decrease to attain their minima in the upper third of the CBL. Afterwards, the variances increase again to attain secondary maxima in the entrainment zone. Above the CBL the variances of horizontal wind components rest at their numerical minima. At the culmination of CBL evolution, the variance of the vertical velocity (Fig. 3f) attains a well-defined maximum in the lower third of the CBL. In opposite to horizontal wind variances, the vertical wind variance assumes a minimum at the surface half level, where large eddies just form and start to rise thereby turning around the horizontal flow into vertical direction. In

the course of the day, the horizontal and vertical wind variances attain their maxima in the early afternoon, which corresponds to the diurnal maximum of TKE and turbulent length scale in the middle of the CBL leading to a maximum of the turbulent exchange. In Fig. 3c and e the components of the turbulent momentum fluxes, i.e., $\overline{w'u'}$ and $\overline{w'v'}$, are shown. In the CBL, the turbulent momentum fluxes are negative, i.e., they are downward directed with maximum negative values occuring in the lowermost model layers. The friction due to surface roughness serves as a sink for momentum. The cross-correlation of momentum fluctuations $\overline{u'v'}$ as shown in Fig. 3b is slightly positive in most parts of the CBL except for the lowest half level and the entrainment zone, where momentum components fluctuations are clearly anticorrelated. In the bulk of the CBL positive or negative u-wind fluctuations, respectively, correspondingly coincide with positive or negative v-wind fluctuations, respectively.

(b) Comparison with reference results

The vertical distribution of wind variances $\overline{u'u'}$, $\overline{v'v'}$, $\overline{w'w'}$ at the time of well-developed CBL is very similar to that obtained from large-eddy simulations (LES) of the free convective atmospheric boundary layer with an overlying capping inversion such as performed by Mason (1989, Figs. 5b, 6b, 18 for $\overline{u'u'}$), Mason (1989, Figs. 5a, 6a, 7, 8, 18 for $\overline{w'w'}$), Sorbjan (1996a, Fig. 15 for $\overline{u'u'}$, $\overline{v'v'}$, $\overline{w'w'}$), Sorbjan (1996b, Fig. 7 for $\overline{u'u'}$, $\overline{w'w'}$), Sullivan et al. (1998, Fig. 4 for $\overline{u'u'}$, $\overline{v'v'}$, $\overline{w'w'}$), Cuijpers and Holtslag (1998, Fig. 5 for $\overline{w'w'}$ in the dry CBL driven by surface heat flux), Muschinski et al. (1999, Fig. 8 for $\overline{w'w'}$), or even from LES of the slightly convective, strong shear PBL for z/z_i<0.25 performed by Sullivan et al. (1996, Fig. 8 for $\overline{u'u'}$, $\overline{v'v'}$, $\overline{w'w'}$). The behaviour of the vertical wind variance corresponds also to the simulation of CBL using a second-order turbulence closure model performed by Abdella and McFarlane (1997, Fig. 6 for $\overline{w'w'}$ in the buoyancy-driven CBL with small shear, Fig. 13 for $\overline{w'w'}$ in the free-convective case) as well.

The behaviour of the components of turbulent moment flux $\overline{w'u'}$ for z/z_i<0.25 is

qualitatively confirmed by the LES study of Sullivan et al. (1996, Figs. 7, 12 for $\overline{u'w'}$). Further observational results supporting the plausibility of the simulated momentum fluxes can also be found in the second-order turbulence closure study of the dry CBL performed by Abdella and McFarlane (1997, Fig. 9 for $\overline{w'u'}$, $\overline{w'v'}$ in the buoyancy-driven CBL with small shear) that confirms, e.g., the occurrence of positive $\overline{w'v'}$ values within the entrainment layer.

Apart from LES, the behaviour of the wind variances and momentum fluxes aggrees also well with results from a wind tunnel study of turbulent flow structures in the CBL capped by a temperature inversion as performed by Fedorovich et al. (1996, Fig. 5 for $\overline{u'u'}$, $\overline{u'w'}$, $\overline{w'w'}$), which again were compared with existing data sets from atmospheric observations, water tank experiments, and LES by Fedorovich et al. (1996, Fig. 8 for $\overline{u'u'}$, $\overline{w'w'}$);

Compared to LES, water tank or wind tunnel studies, respectively, in situ observations of high-order moments of meteorological variables are relatively spare, e.g., owing to sampling problems. An early observation study of high-order moments in the CBL was carried out by Caughey and Palmer (1979). The present simulations of wind velocity variances agree well with the observations of Caughey and Palmer (1979, Fig. 4a and b for $\overline{u'u'}$, $\overline{v'v'}$, $\overline{w'w'}$ in the free convective case). Casadio et al. (1996) evaluated Doppler-SODAR measurements of convective plume patterns under clear sky conditions and light wind daytime boundary layer over land. The authors showed that characteristic mixed-layer similarity profiles for the daytime convective boundary layer over horizontally homogeneous surfaces can be applied to the nocturnal urban boundary layer during periods of reasonable convective activity as well. The vertical velocity variance simulated here corresponds very well to that observed by Casadio et al. (1996, Fig. 5 for $\overline{w'w'}$), as well as to RADAR-RASS observations in the CBL performed by Wulfmeyer (1999a, Fig. 12 for $\overline{w'w'}$).

3.3.2. Turbulent flux of sensible heat (Fig. 4a)

(a) Simulation results

At night, the turbulent heat is slightly negative. After sunrise, the heat flux increases, exceeding its daily maximum around noon at the surface level. At that time, the entrainment layer with negative turbulent heat flux is well depicted.

(b) Comparison with reference results

The heat flux simulation corresponds very well to flux profiles derived from LES studies of a buoyancy-driven and inversion-capped CBL performed by Mason (1989, Fig. 13 for $\overline{w'\theta'}$), Sorbjan (1996a, Fig. 1 for $\overline{w'\theta'}$), Sorbjan (1996b, Fig. 8 for $\overline{w'\theta'}$), Sullivan et al. (1996, Fig. 11 for $\overline{w'\theta'}$), Cuijpers and Holtslag (1998, Fig. 6 for $\overline{w'\theta'}$), Sullivan et al. (1998, Fig. 3 for $\overline{w'\theta'}$), as well as from second-order turbulence modelling studies of the CBL carried out by Zilitinkevich et al. (1999, Figs. 5–7 for $\overline{w'\theta'}$) and Abdella and McFarlane (1997, Figs. 3, 13 for $\overline{w'\theta'}$).

The simulated heat flux agrees with the results from wind tunnel study of turbulent flow structures in the inversion-capped CBL performed by Fedorovich et al. (1996, Figs. 5, 7 for $\overline{w'T'}$) as well.

Evidences from in situ measurements of the heat flux profile in the CBL that confirm the present simulations were provided by Caughey and Palmer (1979, Fig. 3 for $\overline{w'\theta'}$) and Verver et al. (1997, Fig. 3 for $\overline{w'\theta'}$, see references therein).

3.3.3. Vertical flux of water vapour mixing ratio (Fig. 4b)

(a) Simulation results

During the day, the vertical flux of the water vapour mixing ratio attains its maximum

around noon, whereas the vertical location of that maximum at the surface layer is not that pronounced as for the turbulent heat flux. In the entrainment layer, the turbulent humidity flux is negative. There, spurious oscillations appear, i.e., nonphysical solutions resulting from hyperbolic terms in the gouverning equations of the third-order moments (see part I).

(b) Comparison with reference results

Comparing the humidity flux to LES of the CBL performed by Sorbjan (1996a, Fig. 11 for $\overline{w'q'}$) and to observations as cited by Verver et al. (1997, Fig. 4 for $\overline{w'q'}$, see references therein), the humidity flux in the middle CBL seems to be overestimated. However, the humidity flux in Fig. 3b corresponds well to the result obtained from the third-order turbulence modelling study of the CBL performed by André et al. (1978, Fig. 5 for $\overline{w'q'}$), showing the positive maximum of the humidity flux occurring just below the MLH. There is a need to evaluate the model with respect to the humidity flux prediction. Nevertheless, it is possible to readjust the corresponding parameters in the gouverning humidity flux equation.

3.3.4. Correlation of potential temperature and water vapour mixing ratio (Fig. 4c)

(a) Simulation results

The correlation $\overline{\theta'q'}$ assumes positive values in the lower, and negative values in the upper part of the CBL. In the Prandtl layer, positive temperature fluctuations resulting from rising thermals are associated with corresponding positive humidity fluctuations caused by, e.g., humidity sources such as vegetation or soil moisture. The positive correlation decreases toward the entrainment layer, were positive temperature fluctuations resulting from entrainment of potentially warmer air from the stably stratified free troposphere are associated with negative humidity fluctuations resulting from the entrainment of drier free tropospheric air. Hence, in the entrainment layer,

$\overline{\theta' q'} < 0$.

(b) Comparison with reference results

The $\overline{\theta' q'}$ behaviour agrees well with the commonly accepted CBL perception, e.g., of Stull (1997, p. 373, Eq. (9.6.4k)). The simulated covariance $\overline{\theta' q'}$ corresponds well to that used in the model approach of (Verver et al., 1997, Fig. 7 for $\overline{\theta' q'}$), and it agrees well with further observational findings cited therein. Based on the dependency of $\overline{\theta' q'}$ on height, Easter and Peters (1994, Fig. 6) investigated the effects of turbulent-scale variations on the binary homogeneous nucleation rate for correlated and uncorrelated fluctuations of temperature and water vapour. Due to the anticorrelation of temperature and humidity fluctuations at the CBL top, the turbulence-enhanced nucleation rate can exceed that at mean-state conditions by a factor of up to 70 (Easter and Peters, 1994).

3.3.5. Variance of potential temperature (Fig. 4d)

(a) Simulation results

The vertical $\overline{\theta' \theta'}$ profile reveals two maxima. One maximum occurs in the Prandtl layer and originates from rising thermals in the superadiabatic surface layer. The other one occurs in the entrainment layer originating from overshooting bubbles penetrating into the stably stratified free troposphere. In the upper third of the well-mixed layer $\overline{\theta' \theta'}$ assumes a minimum. During the day, the potential temperature variance are maximal around noon.

(b) Comparison with reference results

The overall behaviour of potential temperature variance agrees well with that obtained from LES of the CBL performed by Sorbjan (1996a, Fig. 9 for $\overline{\theta' \theta'}$), Sorbjan

(1996b, Fig. 6 for $\overline{\theta'\theta'}$), Sullivan et al. (1998, Fig. 5 for $\overline{\theta'\theta'}$) as well as with that from the second-order turbulence modelling study of the CBL performed by Abdella and McFarlane (1997, Fig. 7 for $\overline{\theta'\theta'}$). It also corresponds well to the semi-empirical profile of the potential temperature variance used in the second-order moment closure study of Verver et al. (1997, Fig. 5 for $\overline{\theta'\theta'}$). Around noon, the Z-shape of the $\overline{\theta'\theta'}$ profile in Fig. 4d is confirmed as well by the observed vertical profile of the temperature variance from a wind tunnel study of the CBL performed by Fedorovich et al. (1996, Fig. 9 for $\overline{T'T'}$) and from in situ measured temperature statistics in the CBL performed by Caughey and Palmer (1979, Fig. 5 for $\overline{\theta'\theta'}$).

3.3.6. Humidity variance (Fig. 4e)

(a) Simulation results

The evolution of the humidity variance $\overline{q'q'}$ exhibits a pattern which is very similar to that of $\overline{\theta'\theta'}$. Although the enhanced humidity variance in the Prandtl layer is not as pronounced as for the temperature variance, the double maxima vertical profile is insinuated as well.

(b) Comparison with reference results

The general behaviour of the humidity variance is qualitatively confirmed by the LES studies of the CBL performed by Sorbjan (1996a, Fig. 13 for $\overline{q'q'}$), Sorbjan (1996b, Fig. 11 for $\overline{q'q'}$) as well as by the semi-empirical profile used in the second-order moment closure study performed by Verver et al. (1997, Fig. 6 for $\overline{q'q'}$). Casadio et al. (1996, Fig. 7 for $\overline{q'q'}$) evaluated Raman-LIDAR water vapour measurements in convective plume patterns in the continental CBL that were quite similar to that obtained from LES studies cited before, except for the absence of peaking variances in the Prandtl layer. To note, that the humidity variance is controlled by the flux partition at the

surface, hence potentially being subject of a justification of the parameterization. Very similar to the Raman LIDAR observations of Casadio et al. (1996) are the water vapour DIAL measurements of absolute humidity variance in the CBL performed by Wulfmeyer (1999a, Fig. 14) and Wulfmeyer (1999b, Fig. 2). As their humidity variance profiles start far above the Prandtl layer, no conclusions about the strength of the Prandtl layer variance maximum predicted by LES can be drawn.

3.4. Third-order moments

3.4.1. Vertical flux of vertical velocity variance (Fig. 5a)

(a) Simulation results

The vertical velocity variance flux assumes its maximum around noon in the middle of the CBL. It suddenly decreases in the late afternoon/early evening, when the Prandtl layer buoyancy flux decreases to negative values and CBL turbulence collapses. In the afternoon, the variance flux becomes negative at the lowest main level, indicating that the surface act as a sink for vertical velocity variance.

(b) Comparison with reference results

The vertical behaviour of $\overline{w'w'w'}$ around noon agrees well with the corresponding profiles obtained from the LES studies of the CBL performed by Moeng and Wyngaard (1988, Fig. 12 for $\overline{w'w'w'}$) and Mason (1989, Fig. 9 for $\overline{w'w'w'}$), as well as with that derived from Doppler-SODAR measurements of convective plume patterns in the continental CBL by Casadio et al. (1996, Fig. 6 for $\overline{w'w'w'}$). A further proof for the plausibility of the simulated $\overline{w'w'w'}$ profile is presented in the wind tunnel study of turbulent flow structures in the CBL performed by Fedorovich et al. (1996, Fig. 9b for $\overline{w'w'w'}$).

3.4.2. Vertical flux of heat flux (Fig. 5b)

(a) Simulation results

The flux of heat flux assumes its maximum in the lower third of the CBL around noon, when turbulence is well-developed. In the entrainment layer, the flux of heat flux is negative. While the heat flux tends to balance out the temperature distribution, the flux of heat flux tends to balance out the heat flux distribution and so on.

(b) Comparison with reference results

The profile of the flux of heat flux around noon agrees well with that derived from LES of the CBL performed by Moeng and Wyngaard (1988, Fig. 15 for $\overline{w'w'\theta'}$), and Sorbjan (1996b, Fig. 9 for $\overline{w'w'\theta'}$), furthermore with that used in the second-order moment closure studies of the CBL carried out by Verver et al. (1997, Fig. 10 for $\overline{w'w'\theta'}$), Abdella and McFarlane (1997, Fig. 16 for $\overline{w'w'\theta'}$), and Zilitinkevich et al. (1999, Fig. 3 for $\overline{w'w'\theta'}$) as well.

3.4.3. Vertical flux of temperature variance (Fig. 5c)

(a) Simulation results

The vertical distribution of $\overline{w'\theta'\theta'}$ reveals a typical S-shape structure, i.e., a positive maximum near the CBL top, a negative minium in the entrainment layer, a positive maximum in the lower quarter of the CBL, and a near zero minimum in the Prandtl layer. This S-shape profile is most pronounced when the turbulence is well-developed, i.e., around noon.

(b) Comparison with reference results

The vertical profile of $\overline{w'\theta'\theta'}$ is very similar to that derived from LES of the CBL performed by Moeng and Wyngaard (1988, Fig. 15 for $\overline{w'\theta'\theta'}$), and Sorbjan (1996b, Fig. 10 for $\overline{w'\theta'\theta'}$), as well as to that from second-order moment closure studies of the CBL performed by Verver et al. (1997, Fig. 9 for $\overline{w'\theta'\theta'}$), and Abdella and McFarlane (1997, Fig. 16 for $\overline{w'\theta'\theta'}$). Differences between the various profile can be easily related to corresponding differences of the forcing at lower and upper model boundary (model setup).

3.4.4. Triple correlation of potential temperature (Fig. 5d)

(a) Simulation results

Around noon, the profile of $\overline{\theta'\theta'\theta'}$ assumes a weak positive maximum in the Prandtl layer, decreasing above to a weak positive minimum, afterwards increasing above to assume an absolute maximum just below the CBL top, and changing over afterwards to reach an absolute negative minimum in the entrainment layer.

(b) Comparison with reference results

This profile is in qualitatively good agreement with previous findings, as seen from the LES of the CBL performed by Sorbjan (1996a, Fig. 10 for $\overline{\theta'\theta'\theta'}$) and from the second-order moment closure study of the CBL performed by Verver et al. (1997, Fig. 8 for $\overline{\theta'\theta'\theta'}$). Observed differences in the entrainment layer ($\overline{\theta'\theta'\theta'}\leq 0$ in Fig. 10 of Sorbjan (1996a) and ($\overline{\theta'\theta'\theta'}>0$ in Fig. 8 of Verver et al., 1997) are due to the different strength of the CBL top inversion.

3.4.5. Vertical flux of humidity flux (Fig. 5e)

For the following triple correlations, no profiles from previous LES, wind tunnel or CBL observational studies could be found for comparison.
The vertical flux of humidity flux is nearly almost greater than zero, i.e., a downward directed humidity flux is downward transported by CBL turbulence, an upward directed humidity flux is upward transported. The flux of humidity flux assumes its maxium in the upper third of the CBL. It tends to well-mix the humidity flux throughout the CBL. Negative values occur in the entrainment layer. The vertical stripes, periodically appearing in the afternoon entrainment layer, are resulting from non-physically spurious oscillation that were not fully damped.

3.4.6. Vertical flux of humidity variance (Fig. 5f)

The vertical flux of humidity variance assumes a weak positive maximum in the lowest quarter of the CBL and a pronounced one in the entrainment layer. The low-level maxium results from upward transport of enhanced humidity variance in the Prandtl layer by buoyant eddies. The entrainment layer maximum results from upward transport of enhanced humidity variance by large eddies penetrating into the free troposphere.

3.4.7. Vertical flux of potential temperature-water vapour mixing ratio correlation (Fig. 6a)

The flux of temperature-humidity correlation is positive throughout the CBL except for the entrainment layer, where it assumes negative values. Due to commutativity of variables in cross correlation, the flux of double correlation can be interpreted as a double correlation between the vertical component of the turbulent heat flux and the water vapour mixing ratio. Thus, in the lower third of the CBL the turbulent heat flux is positively correlated with water vapour mixing ratio, i.e., the upward directed turbulent heat flux originated in the Prandtl layer is associated with positive humidity fluctuations. In

the entrainment layer both terms are anticorrelated. There, buoyant eddies penetrating into the free troposphere ($w'>0$) are correlated with positive fluctuations of potential temperature originating from warm thermals ($\theta'>0$) and negative fluctuations of water vapour mixing ratio originating from dry free tropospheric air ($q'<0$). This results in a pronounced negative minimum of $\overline{w'\theta'q'}$ in the entrainment layer.

3.4.8. Correlation of potential temperature variance and water vapour mixing ratio (Fig. 6b) and correlation of water vapour mixing ratio variance and potential temperature (Fig. 6c)

The triple correlations $\overline{\theta'\theta'q'}$ and $\overline{\theta'q'q'}$ have a double-peak profile structure throughout the CBL. Just below the CBL top, penetrating warm thermals ($\theta'>0$) are associated with temperature-humidity anticorrelation ($\theta'q'<0$) resulting in $\overline{\theta'\theta'q'}<0$. Just above, $\theta'q'$ becomes greater zero, hence leading to $\overline{\theta'\theta'q'}>0$. For $\overline{\theta'q'q'}$ the conditions are reversed. Just below the CBL top, intrusions of dry free tropospheric air ($q'<0$) are associated with temperature-humidity anticorrelation ($\theta'q'<0$) resulting in $\overline{\theta'q'q'}>0$. Just above $\overline{\theta'q'q'}$ becomes greater zero due to $\theta'q'>0$.

3.4.9. Triple correlation of water vapour mixing ratio (Fig. 6d)

The double-peak structure in the entrainment layer can also be seen in the $\overline{q'q'q'}$ profile. Just below the CBL top $\overline{q'q'q'}$ becomes lower, just above the CBL top greater than zero. To note, that the strength of the double-peak pattern in the entrainment layer profiles of $\overline{\theta'\theta'\theta'}$ (Fig. 5d), $\overline{\theta'\theta'q'}$ (Fig. 6b), $\overline{\theta'q'q'}$ (Fig. 6c), and $\overline{q'q'q'}$ (Fig. 6d) are directly related to the strength of the capping inversion. The modelling of second-order and third-order moments just there deserves further tuning of the parameterization, and perhaps, of the numerical scheme as well. For finetuning, additional reference data of third-order moments derived from LES, wind tunnel study and/or in situ observations are necessary.

ACPD
5, 11489–11515, 2005

3.5. Prandtl layer properties

The turbulent vertical fluxes of sensible heat, latent heat and momentum in the Prandtl layer are depicted in Fig. 7a–c. At night, the turbulent heat flux is negative, i.e., directed toward the surface (Fig. 7a). After sunrise it increases, assuming its maximum around noon. The humidity flux is negative at night as well, i.e., deposition of humidity occurs (daw)(Fig. 7a). When the sun elevates above the horizon, a part of the incoming solar radiation contributes to evaporation, leading to an increase of the humidity flux synchronously to the diurnal variation of the sensible heat flux. The variance of the vertical velocity in the Prandtl layer is shown in Fig. 7b. The sharp drop of the initial value of $\overline{w'w'}$ at the beginning is related to the adaptation phase of the model. Afterwards, $\overline{w'w'}$ increases in the course of the day, exceeding its maximum in the early afternoon, when CBL turbulence is well-developed. The vertical fluxes of the horizontal wind components in the Prandtl layer, $\overline{w'u'}$ and $\overline{w'v'}$, are negative, i.e., owing to aerodynamic roughness the surface acts as a sink for the momentum flux. The temperature and humidity evolution in the course of the day is shown in Fig. 7c. The temperature minimum and the maximum of the water vapour ratio coincide and appear just before sunrise. Afterwards, the Prandt layer temperature rises due to increasing flux of sensible heat. The rise of water vapour mixing ratio during the day due to increasing humidity flux is superimposed by its turbulence-induced dilution. This results in a solely weak secondary maximum of $\overline{q}$ around noon.

4. Summary and conclusion

Simulated first-, second- and third-order moments of the CBL agree very well with results obtained from from LES and wind tunnel studies as well as with available in situ observations and remote sensing data. Especially with respect to second-order moments, Doppler-SODAR, RADAR-RASS, and water vapour DIAL provide a high potential of information for model evaluation. Small differences in the behaviour of some

third-order moments near the entrainment layer can be related to differences in the strength of the CBL top inversion. With respect to these differences it should be notet that a part of the reference data directly confirms the present simulations, another does not. Hence, further investigations are deserved to calibrate the model. High-order moments for which no comparative reference results are available show a physically plausible behaviour. Altogether, the simulation performed here is a suitable base to study NPF in the CBL, especially to examine previous hypothesis on the role of turbulence in burst formation. As the gouverning equations for the second-order and third-order moments of meteorological variables are physically and algorithmically identical to the non-reactive part of the chemical and aerosol dynamical system, the conducted model examination for meteorological flow properties may serve, to some degree, as a control of the computational feasibility of third-order modelling of physico-chemical and aerosol properties as well. Nevertheless, the turbulence model deserves further fine tuning, explicit verification/validation, and model intercomparison studies using high-order moments that are both directly derived from in situ observations as well as indirectly derived from remote sensing measurements. Based on the CBL simulation presented here, in part III and IV a conceptual study on NPF in the anthropogenically influenced CBL will be performed. The results will be compared with a number of in situ measurements of NPF under very different conditions to verify or falsify, respectively, a state-of-the-art hypothesis on the role of turbulence in NPF.

References

Abdella, K. and McFarlane, N.: A new-second order turbulence closure scheme for the planetary boundary layer, J. Atmos. Sci., 54, 1850–1867, 1997. 11494, 11495, 11496, 11499, 11501, 11502

André, J. C., De Moor, G., Lacarrère, P., Therry, G., and Du Vachat, R.: Modeling the 24-hour evolution of the mean and turbulent structures of the planetary boundary layer, J. Atmos. Sci., 35, 1861–1883, 1978. 11497

Casadio, S., Sarra, A. D., Fiocco, G., Fuá, D., Lena, F., and Rao, M. P.: Convective characteris-

tics of the nocturnal urban boundary layer as observed with Doppler sodar and Raman lidar, Boundary-Layer Meteor., 79, 375–391, 1996. 11495, 11499, 11500
Caughey, S. J. and Palmer, S. G.: Some aspects of turbulence structure through the depth of the convective boundary layer, Quart. J. Roy. Meteor. Soc., 105, 811–827, 1979. 11495, 11496, 11499
Cohn, S. A. and Angevine, W. M.: Boundary layer height and entrainment zone thickness measured by Lidars and wind-profiling Radars, J. Appl. Meteor., 39, 1233–1247, 2000. 11492
Cuijpers, J. W. M. and Holtslag, A. A. M.: Impact of skewness and nonlocal effects on scalar and buoyancy fluxes in convective boundary layers, J. Atmos. Sci., 55, 151–162, 1998. 11494, 11496
Easter, R. C. and Peters, L. K.: Binary homogeneous nucleation: Temperature and relative humidity fluctuations, nonlinearity, and aspects of new particle production in the atmosphere, J. Appl. Meteor., 33, 775–784, 1994. 11498
Fedorovich, E., Kaiser, R., Rau, M., and Plate, E.: Wind tunnel study of turbulent flow structure in the convective boundary layer capped by a temperature inversion, J. Atmos. Sci., 53, 1273–1289, 1996. 11495, 11496, 11499, 11500
Mason, P. J.: Large-eddy simulation of the convective atmospheric boundary layer, J. Atmos. Sci., 46, 1492–1516, 1989. 11494, 11496, 11500
Moeng, C.-H. and Wyngaard, J. C.: Spectral analysis of large-eddy simulations of the convective boundary layer, J. Atmos. Sci., 45, 3573–3587, 1988. 11500, 11501, 11502
Muschinski, A., Sullivan, P. P., Wuertz, D. B., Hill, R. J., Cohn, S. A., Lenschow, D. H., and Doviak, R. J.: First synthesis of wind-profiler signals on the basis of large-eddy simulation data, Radio Sci., 34, 1437–1459, 1999. 11494
Nilsson, E. D., Rannik, Ü., Kulmala, M., and O'Dowd, C. D.: Effects of continental boundary layer evolution, convection, turbulence and entrainment, on aerosol formation, Tellus, 53B, 441–461, 2001. 11492
Sorbjan, Z.: Numerical study of penetrative and 'solid lid' nonpenetrative convective boundary layer, J. Atmos. Sci., 53, 101–112, 1996a. 11494, 11496, 11497, 11498, 11499, 11502
Sorbjan, Z.: Effects caused by varying the strength of the capping inversion based on a large eddy simulation model of the shear-free convective boundary layer, J. Atmos. Sci., 53, 2015–2024, 1996b. 11494, 11496, 11498, 11499, 11501, 11502
Stull, R. B.: An Introduction to Boundary Layer Meteorology, Kluwer Academic Publishers, Dordrecht/Boston/London, 1997. 11491, 11498

Sullivan, P. P., McWilliams, J. C., and Moeng, C.-H.: A grid nesting method for large-eddy simulation of planetary boundary layer flows, Boundary-Layer Meteor., 80, 167–202, 1996. 11494, 11495, 11496

Sullivan, P. P., Moeng, C.-H., Stevens, B., Lenschow, D. H., and Mayor, S. D.: Structure of the entrainment zone capping the convective atmospheric boundary layer, J. Atmos. Sci., 55, 3042–3064, 1998. 11494, 11496, 11499

Verver, G. H. I., van Dop, H., and Holtslag, A. A. M.: Turbulent mixing of reactive gases in the convective boundary layer, Boundary-Layer Meteor., 85, 197–222, 1997. 11491, 11496, 11497, 11498, 11499, 11501, 11502

Wulfmeyer, V.: Investigation of turbulent processes in the lower troposphere with water vapor DIAL and radar-RASS, J. Atmos. Sci., 56, 1055–1076, 1999a. 11495, 11500

Wulfmeyer, V.: Investigation of humidity skewness and variance profiles in the convective boundary layer and comparison of the latter with large eddy simulation results, J. Atmos. Sci., 56, 1077–1087, 1999b. 11500

Zilitinkevich, S. S., Gryanik, V. M., Lykossov, V. N., and Mironov, D. V.: Third-order transport and nonlocal turbulence closures for convective boundary layers, J. Atmos. Sci., 56, 3463–3477, 1999. 11496, 11501

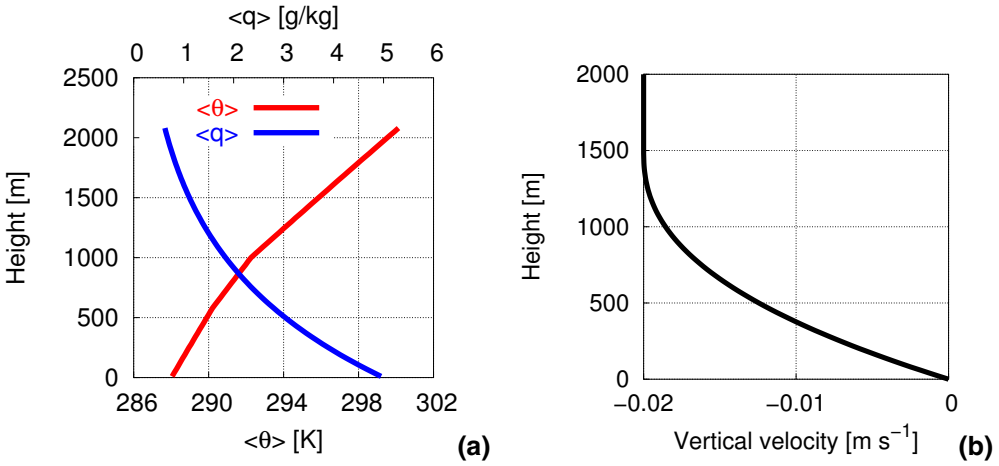

Fig. 1. Initial vertical profiles: **(a)** Potential temperature and water vapour mixing ratio; **(b)** Large-scale subsidence velocity.

ACPD
5, 11489–11515, 2005

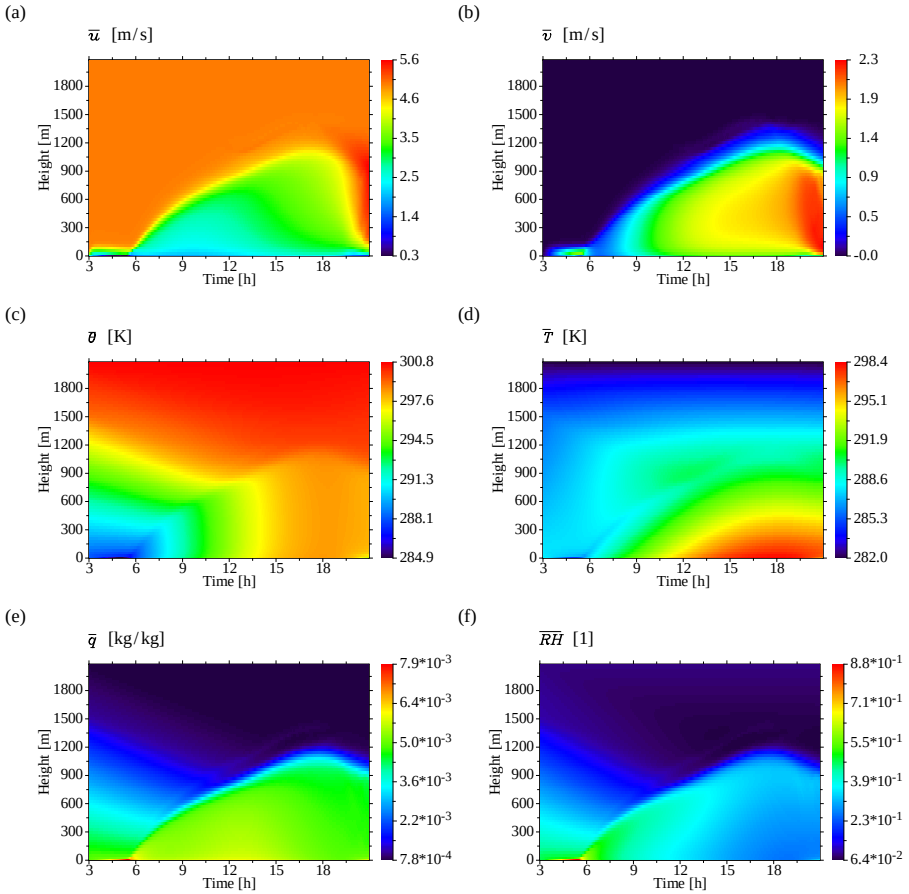

Fig. 2. First-order moments of meteorological variables: **(a)** x-wind; **(b)** y-wind; **(c)** Potential temperature; **(d)** Temperature; **(e)** Water vapour mixing ratio; **(f)** Relative humidity.

ACPD
5, 11489–11515, 2005

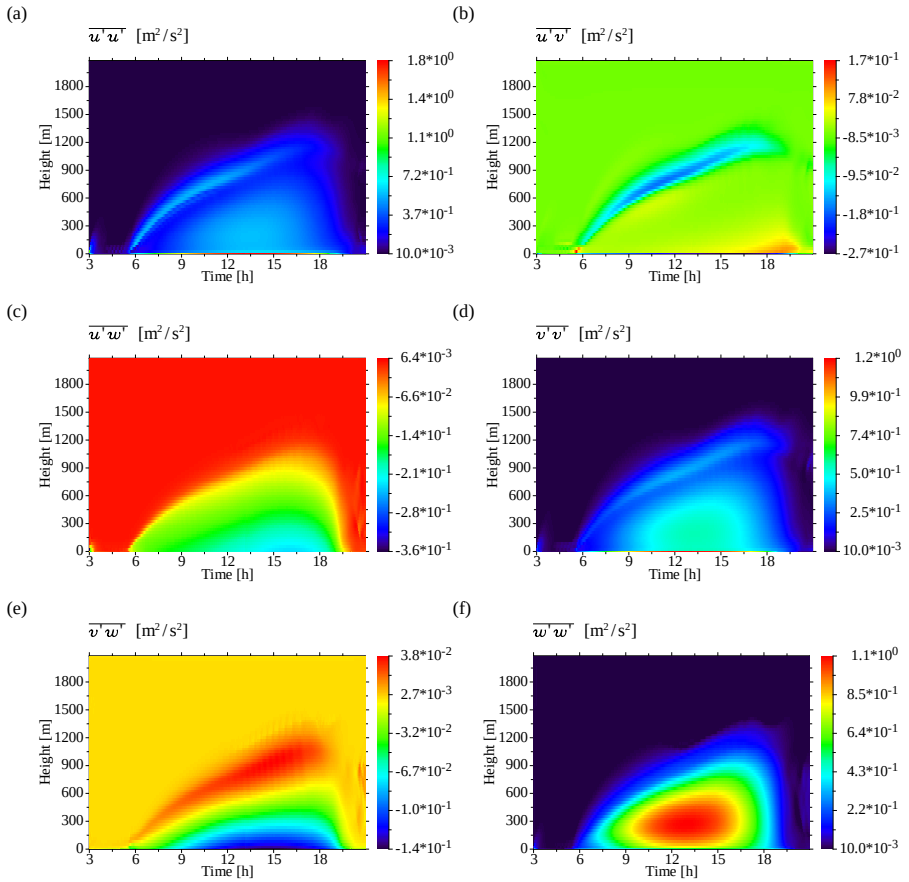

Fig. 3. Components of the Reynolds stress tensor.

ACPD
5, 11489–11515, 2005

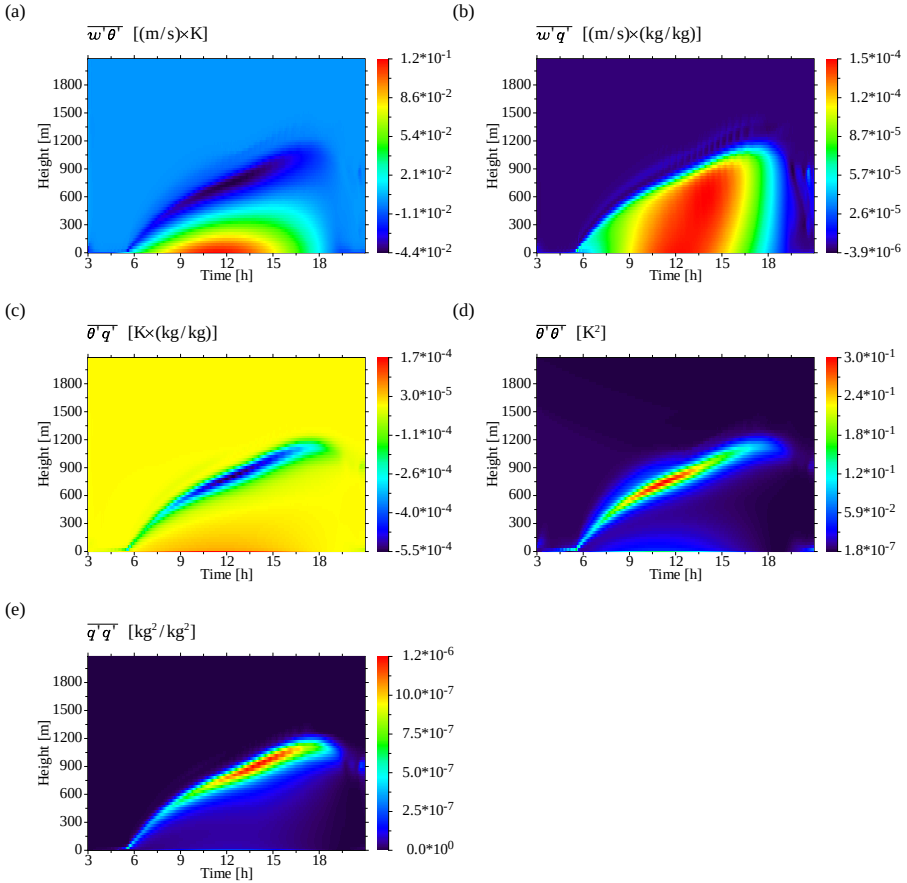

Fig. 4. Fluxes and double-correlations of temperature and water vapour mixing ratio: **(a)** Turbulent vertical flux of potential temperature; **(b)** Turbulent vertical flux of water vapour mixing ratio; **(c)** Covariance of potential temperature and mixing ratio; **(d)** Variance of potential temperature; **(e)** Variance of water vapour mixing ratio.

ACPD
5, 11489–11515, 2005

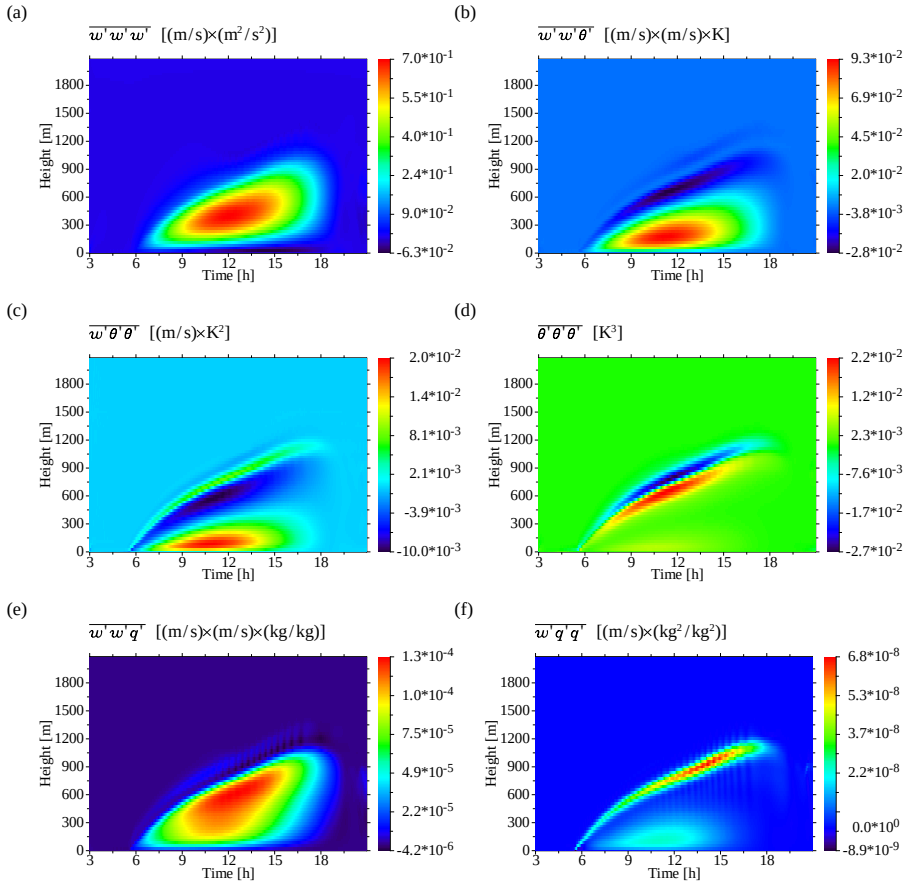

Fig. 5. Triple correlations of meteorological variables: **(a)** Flux of vertical wind variance; **(b)** Flux of turbulent heat flux; **(c)** Flux of variance of potential temperature; **(d)** Third-order moment of potential temperature; **(e)** Flux of turbulent humidity flux; **(f)** Flux of variance of water vapour mixing ratio.

ACPD
5, 11489–11515, 2005

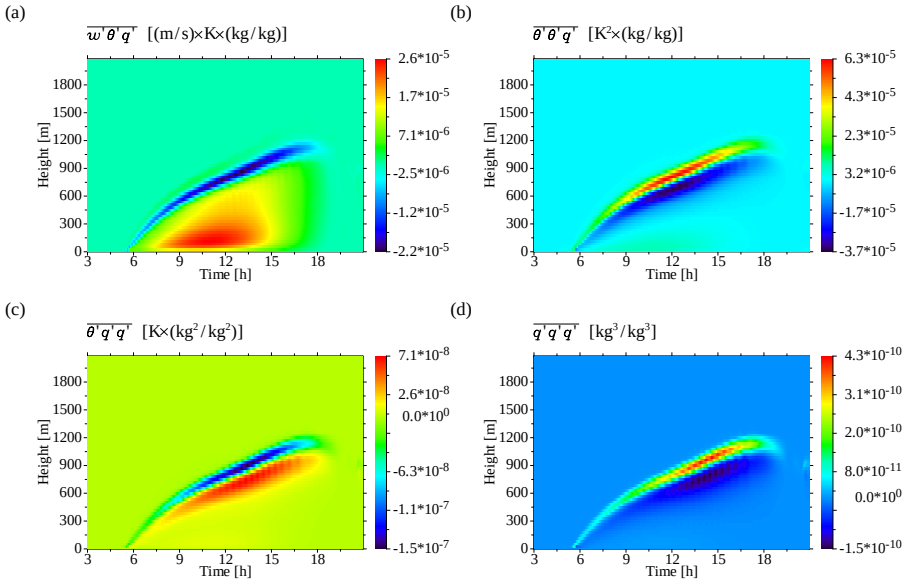

Fig. 6. Triple correlations of temperature and humidity: **(a)** Flux of covariance of potential temperature and mixing ratio; **(b)** Correlation of temperature variance and humidity; **(c)** Correlation of temperature and humidity variance; **(d)** Third-order moment of water vapour mixing ratio.

ACPD
5, 11489–11515, 2005

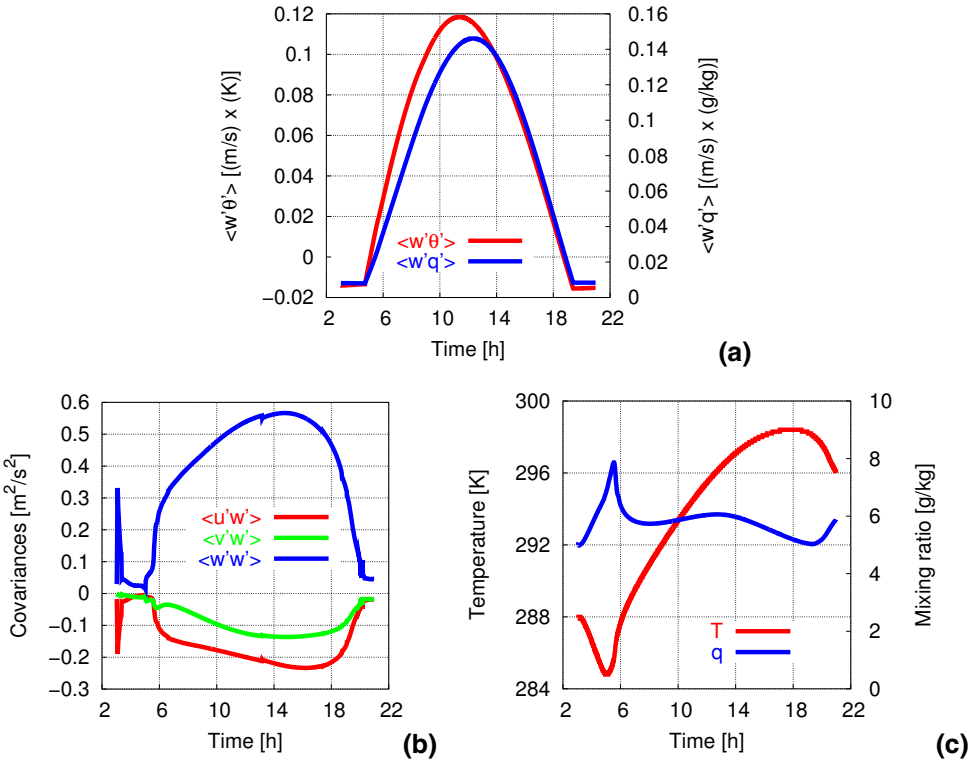

Fig. 7. Time series of meteorological variables in the Prandtl layer: **(a)** Turbulent heat and humidity flux; **(b)** Turbulent moment fluxes; **(c)** Potential temperature and water vapour mixing ratio.

ACPD
5, 11489–11515, 2005